
Please note that this is a preprint listed on EarthArXiv which has not undergone full peer review yet. Subsequent versions may have slightly different content. If accepted, the final version of this manuscript will be available via the ‘Peer-reviewed Publication DOI’ link on the right-hand side of this webpage. Please feel free to contact any of the authors; we welcome the feedback.

1 **Sensitivity, Accuracy and Limits of the Lightweight**
2 **Three-Component SmartSolo Geophone Sensor (5 Hz)**
3 **for Seismological Applications**

4 **Martin Zecka¹, Koen Van Noten¹, Thomas Lecocq¹**

5 ¹Royal Observatory of Belgium, Avenue Circulaire 3, 1180 Brussels, Belgium

6 **Key Points:**

- 7 • instrument tests
8 • nodal systems
9 • SmartSolo
10 • sensor performance

Corresponding author: M. Zeckra, martin.zeckra@seismology.be

11 **Abstract**

12 The use of Nodal systems based on autonomous geophone-based instruments entered the
13 field of Seismology only recently. These lightweight solutions revolutionized seismolog-
14 ical fieldwork through lightweight and wholistic instruments that are faster to deploy and
15 easier to handle. The IGU-16HR series of SmartSolo® is one example, but yet lacking
16 a thorough lab-based performance analysis. Here, we fill the knowledge gap, by perform-
17 ing a series of lab and field-based tests that focus on the sensors performance. The in-
18 vestigated parameters are the instruments transfer function, self-noise and overall per-
19 formance to classical seismometer-based instruments. In the real-world application we
20 show examples of H/V measurements of ambient vibrations in urban environments and
21 the performance ranges with teleseismic waveform recordings. Under lab conditions, the
22 nodal systems perform equally well as standard seismometers (e.g., Lennartz 3D/5s), even
23 in the frequency range down to 0.2Hz, way below their natural frequency. The restitu-
24 tion can be carried out correctly with manufacturer given transfer function. At least for
25 the vertical component, the instruments self-noise reaches the lower boundary of the global
26 minimum noise level, confirming the ability to properly record teleseismic phases down
27 to 0.1 Hz. In ambient noise studies the instrument limits are already reached at 0.8 Hz,
28 but still resolve the fundamental frequencies within the methods uncertainty ranges, based
29 on classical instrument data. These versatile and easy-to-use nodal systems are useful
30 and reliable for a wide range of seismological applications. In addition, their installation
31 is faster and reduced prices open the doors towards Large N installations and research
32 studies for groups that face limited financial budgets.

33 **Introduction**

34 Recent developments in seismological research have seen tremendous increases in
35 sheer size of data throughout the last decade (Quinteros et al., 2021; Arrowsmith et al.,
36 2022). This evolution has been accompanied by increasing computational power enabling
37 the processing of such large data-sets (Ahrens et al., 2011; Bozdog et al., 2014; MacCarthy
38 et al., 2020) and the introduction of Machine Learning techniques for seismological data
39 processing (Bergen et al., 2019; Kong et al., 2019; Arrowsmith et al., 2022). On the hard-
40 ware side, the introduction of low-cost geophone sensors (e.g., Raspberry Shake) often
41 in combination with wholistic software/hardware solutions enabled data recording in un-
42 precedented quantity of stations and for non-scientific audiences, for which the term "cit-

43 izen science” has been introduced (Chen et al., 2020; Subedi et al., 2020; De Plaen et
 44 al., 2021; Calais et al., 2022). While the use of such low-cost instrument is limited and
 45 cannot cover the full range of seismological methods (Anthony et al., 2019), integrated
 46 nodal systems bear the potential to present a cost-efficient compromise of the performance
 47 in between citizen instruments and classical seismological sensors.

48 Nodal systems are common practice in active seismic experiments for exploration
 49 of hydrocarbon and other resources (Dean et al., 2018), in which numerous geophones
 50 (mostly single component instruments) are regularly spaced over a site of interest record-
 51 ing subsurface reflections of actively induced signals (e.g., explosive or sweep). Besides
 52 extending to three-component instruments, latest developments in geophone sensors for
 53 nodal installations saw major efforts in enhancing the level of autarky. To overcome is-
 54 sues of power supply, communication and time accuracy in remote locations, integrated
 55 nodal systems eliminate cable-based solutions and incorporate digitizer, data storage,
 56 GPS and battery in a single acquisition unit (Dean & Sweeney, 2019). The first com-
 57 mercially available node that also enabled continuous data recording was the Fairfield
 58 ZLand node (A. T. Ringler et al., 2018). This instrument is also eligible to be used for
 59 seismological research questions. With a fraction of the purchasing costs compared to
 60 standard seismological acquisition systems, the installation of so-called Large N arrays
 61 with 100s to 1000s of nodes became possible (Hand, 2014; Karplus & Schmandt, 2018;
 62 Roux et al., 2018; Brenguier et al., 2015). One of the first installations of such kind was
 63 realized in the Los Angeles basin with $\sim 13,000$ seismic stations covering an area of 16
 64 x 16 km with three separated arrays and equidistant sensor spacing of 100m that enabled
 65 unprecedented spatial sampling of wavefield and site-characteristics (Castellanos & Clay-
 66 ton, 2021).

67 SmartSolo® recently released their IGU-16 series instruments. These geophone
 68 instruments with a 5 Hz natural frequency are available as single (IGU-16 1C) or three-
 69 component (IGU16-HR 3C) sensors and are equipped with 24 bits digitizers and GPS.
 70 Batteries are modular and available as High Capacity Battery or Standard Capacity Bat-
 71 tery Packs which, together with the sensor, eventually provides a single, closed casing
 72 sensor. The total weight of the 3C (2.4 kg high capacity, 1.7 kg standard capacity bat-
 73 tery) and size (10.3 x 9.5 x 18.7 cm) outperforms classical seismometer-digitizer set-ups.
 74 During the installation of larger surveys, the operator profits from the reduced man-power
 75 and time necessary. Due to the modular design of the nodes that allows the replacement

76 of their spike base with a tripod battery base, these sensors' potential use becomes in-
 77 dependent from the available surface structure in the survey area, i.e., urban environ-
 78 ments with a high degree of sealing. In the last years, the SmartSolo node series have
 79 been increasingly used for Large N installations in the field of passive seismology (e.g.
 80 Obermann et al., 2022; Chmiel et al., 2019).

81 So far, a comprehensive study identifying the capabilities of geophone-based node
 82 sensors for seismological purposes has only been performed for the Fairfield ZLand sen-
 83 sors (A. T. Ringler et al., 2018), but is yet unavailable for the SmartSolo sensors. In this
 84 study we evaluate the SmartSolo instruments characteristics, performance and limits in
 85 order to justify their use in a variety of seismological applications. In a set of lab-based
 86 experiments we identify the sensors' transfer function, control the manufacturer's given
 87 poles and zeros, check the self-noise level, and compare the sensors with well-calibrated
 88 seismometers. After that, we show the performance of the sensors during field installa-
 89 tions with two examples focusing on teleseismic waveforms and ambient seismic noise
 90 measurements.

91 **Instrument tests**

92 **Instrument response derived from coherent waveforms**

93 In the recording of ground shaking, a seismic sensor acts as a filter in the sense of
 94 a linear, time-invariant system (LTI) (Scherbaum, 2006) when translating it into elec-
 95 tric voltages as an output signal. This alternation from input to output signal is repre-
 96 sented through the system's frequency response function or the transfer function. The
 97 quantitative description of the LTI then allows us to restore the original input signal by
 98 applying signal restitution to the obtained waveforms without further knowledge of the
 99 physical processes going on inside the filter (Scherbaum, 2006). The transfer function
 100 is then characterized by the complex poles and zeros.

101 Havskov & Alguacil (2015) have shown that it is possible to estimate the transfer
 102 function of a seismometer by using the natural vibrations of the ground as a shaking ta-
 103 ble recorded with two closely installed sensors. For the SmartSolo sensors, the output
 104 signal is expected to be contaminated by instrument noise and thus, we applied the cross-
 105 spectrum method (Eq. 1). In this method, the output of seismometer 1 is the input of
 106 seismometer 2 as a linear system that presents a transfer function in the form of:

$$T_2(\omega) = T_1(\omega) \frac{P_{21}(\omega)}{P_{11}(\omega)} \quad (1)$$

107 with P_{21} as the cross-spectrum between the outputs of both sensors and P_{11} as the au-
 108 topower spectrum of the output of sensor 1. Under the assumption the instrument re-
 109 sponse (as poles and zeros) given by the manufacturer is correct for sensor 1, we can es-
 110 timate the unknown response of sensor 2. This is repeated for all instrument pairs.

111 The estimation of the instrument response parameters represented by its poles and
 112 zeros is a non-linear operation. Therefore, T_2 is identified through the optimization of
 113 the poles and zeros and fitting the theoretical response function to the observed trans-
 114 fer function presented in equation 1. The misfit function of the optimization is repre-
 115 sented by the complex L2-norm.

116 In order to obtain highly correlated ground motions, 24 3C nodes have been closely
 117 co-located (in a so called ‘huddle’, Fig. 1c) in a regular grid of 1m x 1m overall exten-
 118 sion close to the Uccle permanent station of the Belgian seismic network (international
 119 code BE.UCC, Royal Observatory of Belgium, 1985). The location within Brussels as-
 120 sured a high noise level. During the recording period a teleseismic earthquake could be
 121 recorded (M7.3, Japan, GEOFON Data Centre, 1993) that further guarantees strong cor-
 122 relation of the obtained wavefield.

123 The resulting poles for the instrument response estimation strongly converge to-
 124 wards the values given by the manufacturer ($-22.2111-22.2178i$, $-22.2111+22.2178i$),
 125 with half of the estimated transfer functions obtaining misfits below 5%. The weighted
 126 mean for poles below this misfit threshold differs by $-0.0559 \mp 0.0552i$ from the man-
 127 ufacturer given values. Considering only the results with misfits below 2%, the poles dif-
 128 fer by $-0.0162 \mp 0.0158i$. Stronger misfit of the resulting transfer functions are foremost
 129 proportional to intersensor distances as the higher frequency sections of the recorded noise
 130 spectra de-correlate with increasing distance. This result could be reproduced for the
 131 horizontal components as well, with an overall greater spread of high misfit poles and
 132 zeros. This is likely due to the higher self-noise of the horizontal components (section
 133 2.2) that leads to less coherent waveforms, as they show lower signal-to-noise ratio of the
 134 teleseismic phases and are more affected by tilt of the sensor that reduces the overall sen-
 135 sitivity. However, the limitation to results with misfits below 5% or 2% leads to the same

136 range of differences between manufacturer and estimated poles and zeros as determined
 137 for the vertical component.

poles	$-22.2111 - 22.2178i$	$-22.2111 + 22.2178i$
zeros	$0i$	$0i$
sensitivity (@0 gain)	$76.7e3 \frac{mV}{\frac{m}{s}}$	
digitizer gain	3355.4432	

Table 1. Instrument Response for a SmartSolo IGU-16HR-3C node represented by Poles and Zeros.

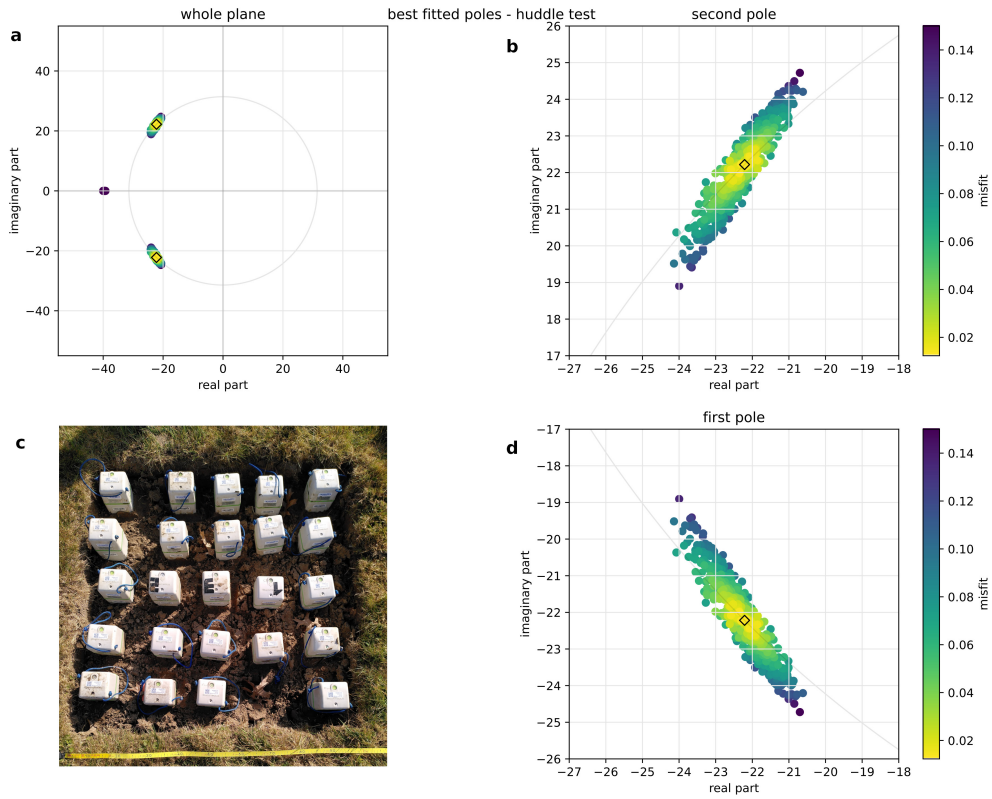


Figure 1. The resulting poles of the SmartSolo nodes huddle test, color-coded by misfit from the manufacturer’s values, shown by the diamond marker. a) result shown over the whole complex plane that has been defined as the solution space in the inversion. b) and d) close-up view of the two poles. c) 24 nodes co-located during the huddle test. Note the slightly imperfect installation, contributing negatively to the misfit values.

138 **Instrument self-noise and long-term noise stability**

139 The experiment set-up presented in figure 1c of 24 co-located SmartSolo 3C instru-
 140 ments allowed us to apply the three instrument approach of Sleeman et al. (2006) to iden-
 141 tify the instrument’s self noise based on a common, coherent input data. Here, we rely
 142 on the analysis of actual ground motion recordings during the self-noise test. As the sen-
 143 sor and digitizer are located within the same casing, we cannot measure their self-noise
 144 independently and the full recording system combining both sensor and digitizer is an-
 145 alyzed. For the most part, the self noise of digitizers lies up to 20dB below the self noise
 146 of the sensors A. T. Ringler et al. (2014) and thus we assume that the obtained noise
 147 spectra will reflect only the sensor’s self noise.

148 The comparison was performed for each instrument (i) using the two closest neigh-
 149 boring sensors of the grid (j, k). Similar to the huddle test, the use of the cross-spectrum
 150 (P_{ji}, P_{ik} , etc.) between the sensors eliminates the sensor’s transfer functions and noise
 151 cross-spectra. The systems self-noise autospectrum (N_{ii}) then can be expressed solely
 152 through power- and cross-spectra of the obtained output of the three sensors (i, j, k)
 153 under the assumption of a common recording input as follows:

$$N_{ii} = P_{ii} - P_{ji} \cdot \frac{P_{ik}}{P_{jk}} \quad (2)$$

154 In order to retain comparability of the experiment outcome of A. T. Ringler et al.
 155 (2018) in which the authors performed a lab test for the Fairfield nodes on a shaking ta-
 156 ble and comparison with broadband sensors, we apply the same Fourier transformation
 157 parameters, prior downsampling (decimate from 250 to 50 Hz), and moving average to
 158 smooth the resulting spectra. The input data is a 1-hr period at a Thursday night (2022-
 159 03-17 01:30:00 UTC) in order to minimize the environmental noise close to the BE.UCCS
 160 station (lat 50.797, lon 4.36) in an open field as the spike at the bases could not be re-
 161 moved. In order to reduce errors propagating from transfer functions uncertainties, the
 162 input waveforms have been restituted (A. Ringler et al., 2011).

163 The resulting self-noise is stable between 0.7 to 15 Hz at around -160 dB (figure
 164 2), just above the global lower noise model (NLNM, Peterson, 1993). For lower frequen-
 165 cies the self-noise is steadily increasing but remains below the NLNM until 0.2 Hz. For
 166 higher frequencies the self-noise is decreasing and shows stronger instabilities in the spec-

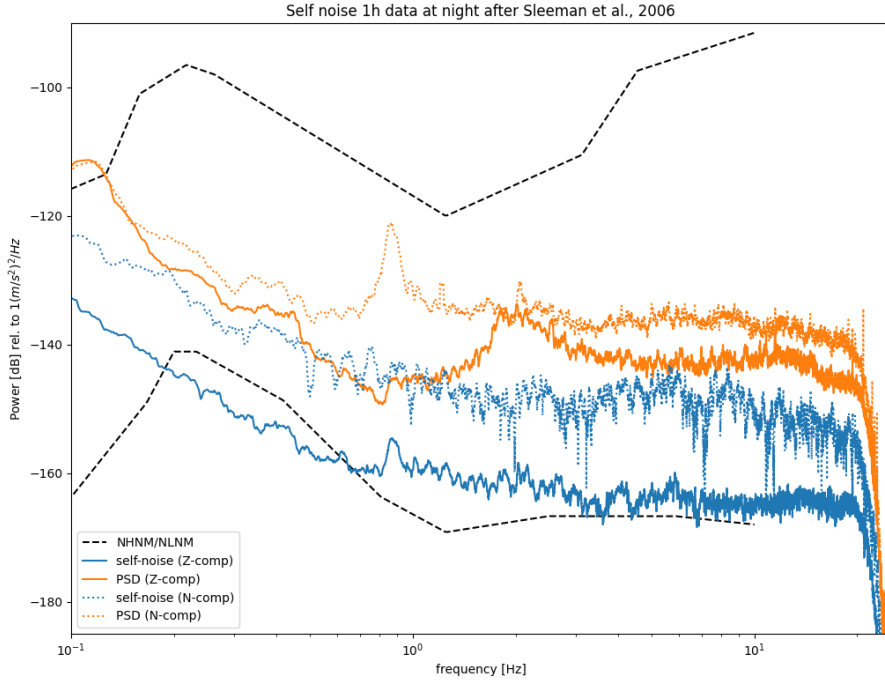


Figure 2. Outcome of the self-noise test following Sleeman et al. (2006). Blue curve is the estimated system self noise for a SmartSolo 3C sensor (vertical component). Orange curve shows the power spectrum of the recorded ground motion. The dashed colored lines show the equivalent for the North component. The black, dashed lines give the upper and lower global noise model bounds (Peterson, 1993).

167 tral amplitudes. The overall shape of the noise spectrum is comparable to the Fairfield
 168 nodes (A. T. Ringler et al., 2018), while for the frequency range < 2 Hz the SmartSolo
 169 node outperforms the Fairfield sensor. This observation underlines the good sensitivity
 170 of the SmartSolo nodes for a seismological purpose as a passive sensor for temporal in-
 171 stallations for recording ambient seismic noise, detecting local tectonic and/or induced
 172 earthquakes, investigating activity in geothermal fields, and they remain performant over
 173 a large frequency range from 5 s to their chosen Nyquist frequency (here 25 Hz). The
 174 increase in noise level towards the higher periods probably makes them less suitable to
 175 investigate teleseisms, microseism and storms.

176 The horizontal components show on average a 15 dB higher noise level that are more
 177 sensitive to signal distortion due to tilt. The cross- sensor comparison of all 24 installed

178 instruments in the Huddle test experiment shows no major distortions or anomalies for
 179 individual instruments. Only a stronger variability of the noise spectra at higher frequen-
 180 cies above 5 Hz can be observed. We suggest this might be related to the different level
 181 of coupling of each sensor that further introduces incoherencies in the recorded wave-
 182 fields in the ambient noise frequency range. Such incoherence of the input of the three
 183 sensors is then further propagated into the noise spectrum analysis. In future analyses
 184 of the SmartSolo sensors this could be avoided by using a shaking table instead of re-
 185 lying on coherent waveform recordings. The three first generation instruments (indicated
 186 in figure 1c with the letters 1, 2, 3) installed alongside the newest generations show the
 187 same outcome.

188 Comparison with well-calibrated seismometers

	Güralp DM24 + 3ESP	CityShark II + Lennartz 3D	SmartSolo
natural/corner frequency	30 s	5s	5 Hz
sampling frequency	100 Hz	250 Hz	250 Hz
downsampled frequency	50 Hz	50 Hz	50 Hz

Table 2. Overview of seismometer and digitizer combinations with sampling specifications.

189 In a lab-based instrument test, the SmartSolo sensors were compared with well-
 190 calibrated, standard seismometers. The SmartSolo nodes were co-located with (*i*) the
 191 surface sensor of the Uccle station (network station code: BE.UCCS), that consists of
 192 a Güralp DM24/3ESP instrument, and (*ii*) with a Lennartz 3D sensor connected to a
 193 CityShark digitizer (Chatelain et al., 2000) for comparison to a standard instrument that
 194 is used for ambient seismic noise measurements (figure 3). During this experiment, we
 195 also investigated if the modular use of different base set-ups of the Smartsolo nodes al-
 196 ters the recorded noise field. Two different set-ups were tested: (*i*) a 3C node connected
 197 to the High Capacity Battery Pack (gray) on a central spike installed in a sand-filled bucket
 198 and (*ii*) a 3C node connected to the Standard Battery Pack (blue) on a steel tripod base
 199 installed on the floor of the cave next to the listed seismometers above (figure 3).

200 To compare the obtained waveforms in the time and spectral domain, we first re-
 201 moved the instrument responses of all sensors (table 1). The restituted waveforms of all

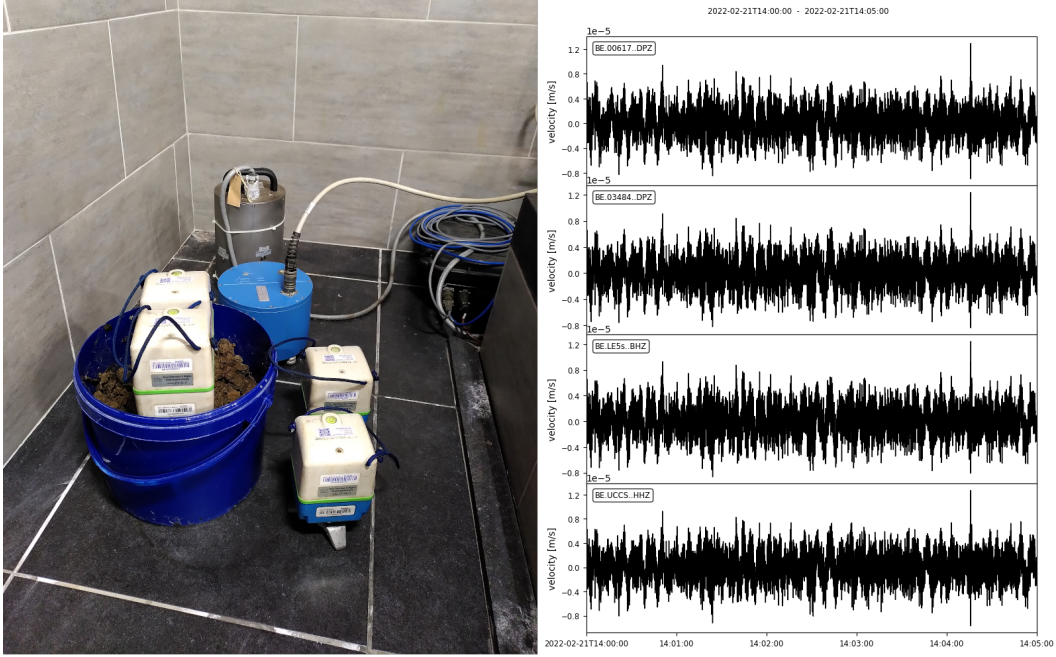


Figure 3. Co-location test of Smartsolo sensors with well-calibrated seismometers. Left: Two nodes each with different base set-ups either on a tripod or with a central spike in a sand-filled bucket, Lennartz LE3D/5s (blue instrument) connect to a Cityshark and Uccle surface station BE.UCCS (gray instrument in the back, Güralp CMG 3ESP). Right: restituted waveforms of all four kinds of sensors: From top to bottom: 1) node in bucket, 2) node on tripod, 3) LE3D/5s, 4) permanent sensor.

202 four sensor types are highly congruent in obtained ground velocity amplitudes and time
 203 accuracy. This congruence demonstrates the accuracy of the nodes' poles and zeros iden-
 204 tified during the huddle test (see section above). In order to quantify the waveform sim-
 205 ilarity, we computed the coherence of all instrument combinations as the normalized cross-
 206 spectra (figure 4).

207 In comparison to the well-calibrated Güralp instrument, the node sensor installed
 208 on a tripod has the highest overall coherence with nearly perfect similarity from 20 Hz
 209 down to 10 s, way below its natural frequency (figure 4). A small deviation is present
 210 between 0.85 and 1.05 Hz that is more evident for the nodes with a central spike, but
 211 the waveform similarity always exceeds a 0.9 coherence. The decreasing coherence above
 212 20 Hz for the SmartSolo sensors appears to be a filter artifact that propagates from the
 213 different decimation applied to the waveforms to result in a common sampling frequency

214 (table 2). For the CityShark with Lennartz instrument the ~ 1 Hz coherence drop is
 215 absent but above 4 Hz the waveform similarity to all other sensors in this test is steadily
 216 decreasing and falls below 0.9 at around 13 Hz. Due to the absence of a lowpass filter
 217 close to the Nyquist frequency of the raw data, we presume the existence of an analog
 218 filter in the CityShark digitizer with a cut-off that starts around 13 Hz and is not included
 219 in the instrument’s transfer function.

220 The instrument comparison in the spectral domain is visualized in figure 4 and was
 221 obtained by dividing the power spectra of all instruments with all other instruments co-
 222 located during the experiment. Similar to the waveform similarity, we obtain flat spec-
 223 tral divisions at the ratio of 1 from $\lesssim 10$ Hz down to less than 10s. Here, the similarity
 224 deviation around ~ 1 Hz of the SmartSolo sensors becomes evident again and also is
 225 more pronounced for the sensors with a central spike installed in a sand-filled bucket.
 226 However, this effect can only be observed for the vertical components and is absent for
 227 the horizontal components. In the low frequency range below 0.2 Hz (remind that the
 228 node’s natural frequency is 5 Hz) the horizontal spectra of the SmartSolo sensors devi-
 229 ate stronger from the spectrum obtained with the well-calibrated instrument as it can
 230 be observed for the vertical components. The deviation from the well-calibrated instru-
 231 ment is even larger for sensors that were installed with a spike in the sand-filled bucket
 232 and thus, results from the fact that the nodes were not fully buried and resulting in poorer
 233 leveling in comparison to the tripod based nodes.

234 **Real-world observations (applications, sensitivity)**

235 **Teleseismic arrivals**

236 In the previous chapter, it was shown that the waveforms obtained with the Smart-
 237 Solo nodes bear the potential to recover ground motion far below their own natural fre-
 238 quency. During two longer term SmartSolo array installations in 2020 and 2022 around
 239 the BE.UCCS station, two teleseismic events in Kermadec (Mw 7.4, June 18, 2020) and
 240 Japan (Mw 7.3, March 16, 2022) respectively occurred during the surveys. To compare
 241 the node’s performance with BE.UCCS, waveforms were first restituted to velocity and
 242 then bandpass filtered between 20 s and 3 s (figure 5).

243 The waveforms of the vertical component of a single Smartsolo sensor perfectly match
 244 the waveforms obtained with a Güralp instrument, with only slightly higher amplitudes

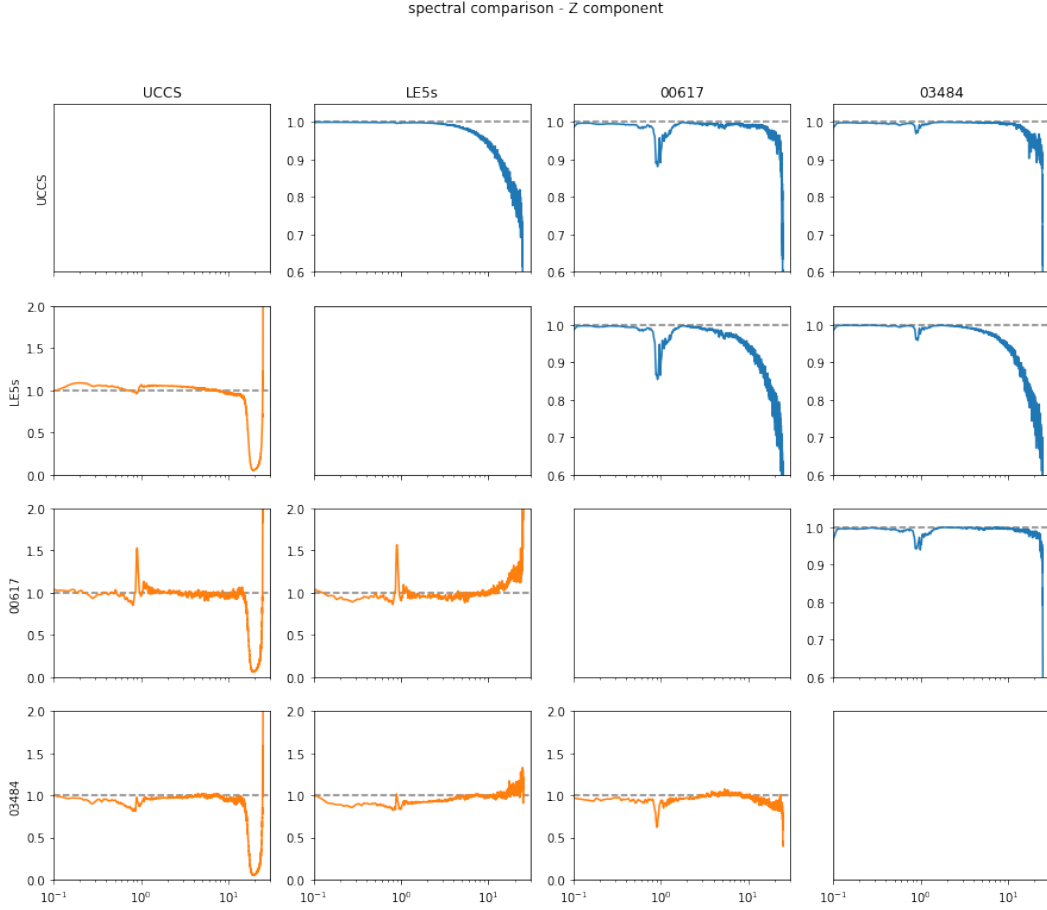


Figure 4. Waveform similarity between different types of sensors. Upper part (blue curves) shows the coherence amplitudes between the different sensors. Lower part (orange curves) gives the spectral divisions of all sensor combinations.

245 for BE.UCCS. For both waveforms, the first arrivals of the body wave phases could be
 246 identified on a single vertical component for both events (PKIKP for Kermadec at 162°
 247 degree distance and PP for Japan at 84° distance). The surface waves of the 2022 Mw
 248 7.3 Japan earthquake could only be retrieved when lowering the bandpass filter down
 249 to 100 s, due to their lower dominant frequencies.

250 The horizontal components have a much reduced sensitivity in the very long pe-
 251 riod range. Thus for the Mw 7.4 Kermadec event, the earthquake can only be identified
 252 by stacking the waveforms of at least 20 nodes. It is important to mention that the sta-
 253 tion BE.UCCS around which the tests were performed is located in the city of Brussels
 254 and possesses one of the highest seismic noise levels in the whole BE network (Lecocq

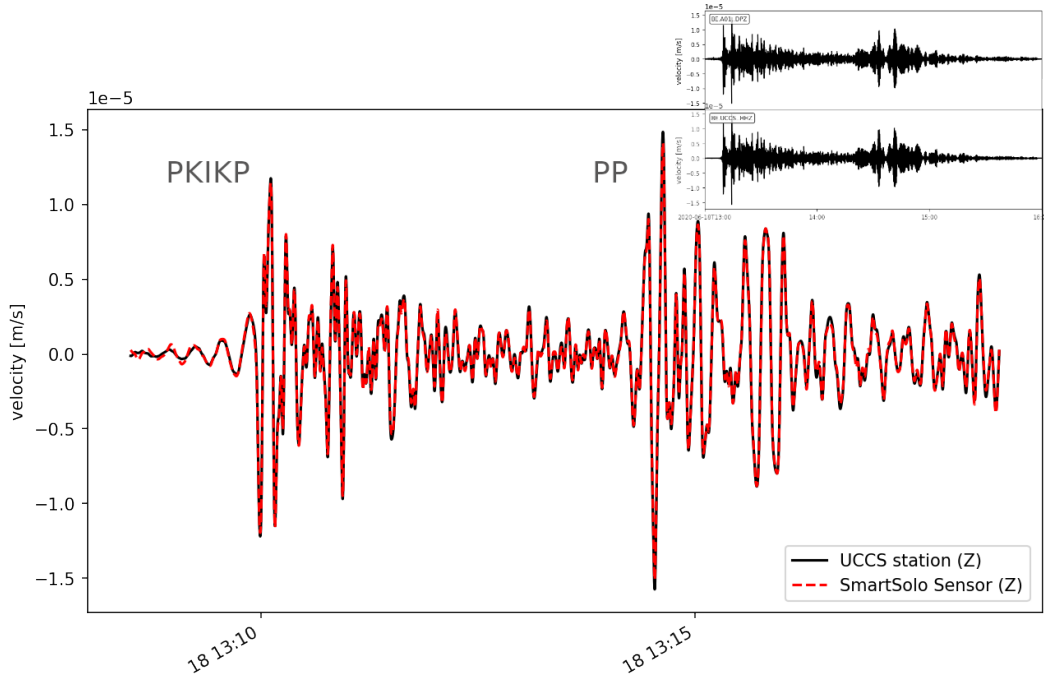


Figure 5. Teleseismic PKIKP and PP phases of the Mw 7.4 Kermadec earthquake (June 18, 2020) recorded with the vertical components at the BE.UCCS station (black) and with a single Smartsolo sensor (red). Both waveforms have been restituted to velocity and filtered between 20 s and 3 s. The inlet shows the full length (3 hours) of the teleseismic earthquake recorded with the SmartSolo Node (top trace) and the Güralp sensor (lower trace).

255 et al., 2020). In contrast, for the Mw 7.3 Japan earthquake, the first arrival S-phases and
 256 the surface waves can already be identified on a single horizontal sensor, but at the same
 257 cost as described before for the vertical component.

258 Ambient noise application

259 The preceding lab-based tests infer a suitable frequency range that justifies to use
 260 the SmartSolo sensors for passive measurements of ambient seismic noise in the frequency
 261 range of 0.2 to 25 Hz. As an example of an ambient noise application, we show three ex-
 262 amples of Horizontal-to-Vertical Spectral Ratio (HVSr) (Nakamura, 1989; Molnar et al.,
 263 2022) surveys in Brussels, Belgium. In the framework of a shallow geothermal feasibil-
 264 ity study, we prospected several sites in Brussels with non-invasive ambient noise obser-
 265 vations prior to drilling. For the region of Brussels (Belgium), a conversion law exists
 266 to estimate the depth to bedrock from fundamental resonance frequency (f_0) values, de-

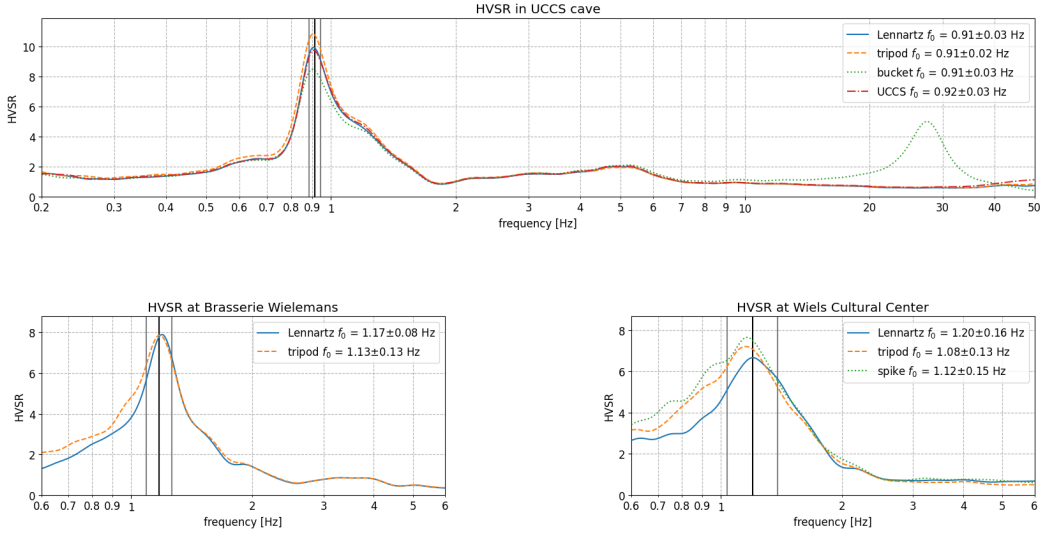


Figure 6. Instrument comparison through H/V analysis at three locations in Brussels. Waveforms have been restituted before the processing. HVSr graph from recordings a) at the location of UCC surface sensor (50.7973N, 4.3605E) from the sensor comparison lab test (fig. 3), with the blue solid line for LE3D-5s with Cityshark, orange dashed line for SmartSolo node on tripod base, green dotted line for node with spike in a sandfilled bucket and red dot-dashed line for Guralp permanent sensor. b) Location of the former Wielemans Brewery (50.8261N, 4.32646E) with LE3D-5s and Smartsolo sensors ~ 10 cm apart. c) Location at the Wiels Cultural Center (50.82453N, 4.3259E) with LE3D-5s, node on tripod and node with spike digged into a grass field. Intersensor distance 5 - 10 m.

267 rived from Horizontal-to-Vertical Spectral Ratio (HVSr) analysis of ambient noise mea-
 268 surements co-located with well logs (Van Noten et al., 2022). In the Brussels capital re-
 269 gion, the main acoustic impedance contrast corresponds to a fundamental frequency range
 270 between 0.6 and 1.6 Hz (Van Noten et al., 2022).

271 At first, the data of the ideal case-study of the instrument comparison test (fig. 3)
 272 have been analyzed using Geopsy (Wathelet et al., 2020). The location of the perma-
 273 nent station (BE.UCCS) within the cave of the Royal Observatory of Belgium (ROB)
 274 reassures constant environmental conditions (e.g., stable temperature, no insulation). The
 275 circular street present around the ROB also provides sufficient distance and azimuthal
 276 coverage of anthropogenic noise sources. In this case study, the same time windows (120s
 277 long) have been used for all co-located instruments and the horizontal components have
 278 been averaged when computing the HVSr spectra. The HVSr spectra for all instruments

(fig. 6a) are congruent for the most parts. The fundamental frequency f_0 can be reproduced by all sensors within 50% of the given uncertainty range (given as one standard deviation in Geopsy). For the HVSR amplitude at the f_0 , the Lennartz seismometer (connected to the City-shark) is comparable to the UCCS, Gralp permanent sensor. The node on the tripod gives a 10% higher and the node in the bucket a 15% lower amplitude value. For frequencies above 13 Hz, the HVSR curve computed from the nodal instrument in the bucket deviates strongly and contains a second peak at 27.5 Hz. We presume this peak is related either to a bad coupling of the spike base in the sand-filled bucket, or to an impedance contrast between the bucket and the tiling floor with its concrete base. Considering the lower HVSR amplitude at f_0 , the former is more likely as tilting shows stronger negative effects of the horizontal than the vertical components according to the manufacturer.

Under real-world conditions we present two examples from the southern part of Brussels. At the first location (fig. 6b), located next to the former *Brasserie Wielemans*, the Lennartz 5s with Cityshark and a SmartSolo node with a tripod base have been placed on a sidewalk, 10 cm apart. The street presents high traffic amounts, including public busses, streetcars and pedestrians passing next to the sensors. The second location, located 200m away from the first case (*Wiels Cultural Center*, fig. 6c) consists of a parking spot next to the same street and a community garden. That allowed us to install the Lennartz and tripod node next to a node with a spike for comparison. Distances between the sensors lie between 5 and 10 m. The f_0 values obtained at both locations are the same on average and given the uncertainties. This is expected as both locations show no elevation difference and have a similar geologic subsurface structure located in the Sennevalley. Above 1.3 Hz the HVSR curves for each location are congruent. The shape of the HV peak for the *Brasserie Wielemans* is sharper and presents smaller uncertainties. The *Wiels* location demonstrates larger variations in f_0 as well as the corresponding amplitude.

The HVSR curves deviate strongly for frequencies below their f_0 peaks. The inspection of all analyzed time windows for the spectral analysis in Geopsy reveals much stronger fluctuation of the individual HVSR curves below 0.8 Hz. This leads to the wider average HVSR peak around f_0 in this frequency range. Below the S-wave resonance frequency the wavefield is dominated by body-waves and nearby sources (Lunedei & Malischewsky, 2015). In a denser urban area, as shown in the two examples, it might be im-

312 possible to decouple the instrument from the noise generating infrastructure (i.e., side-
313 walk of a heavily used street). In addition, noise-receiver distances are short and noise
314 sources are non-stationary. Here, we recommend careful selection of investigation sites
315 with longer recording periods and multiple locations. The impact of the noise instabil-
316 ity below 0.8 Hz could be reduced through restitution of the raw waveform data. This
317 step limits the amplitude differences of the mean HVSR curves as presented in figure 6.

318 The main distinction between the SmartSolo nodes and the classical seismometer-
319 digitizer set-up became obvious in the handling of the hardware during the survey. The
320 integrated node sensors outperform classical instruments in size, weight and usability.
321 In the same time needed for one trained surveyor to install a seismometer-digitizer set-
322 up, a single surveyor can transport and install up to 4 nodes. The use of multiple instru-
323 ments might introduce some redundancy, but allows to capture potential lateral varia-
324 tions over short distances. Especially in urban contexts, additional sensors assure suc-
325 cessful data recordings in cases of unwanted noise sources (e.g., traffic, pumps, etc.), un-
326 known subsurface cavities (e.g., channels, sewers) or bad coupling (see above).

327 **Conclusions**

328 With three different “lab-based” tests using coherent ground motion recordings,
329 we demonstrated the high performance of the 3C SmartSolo sensors (IGU-16HR-3C).
330 The manufacturer given values for the transfer function could be reproduced in the so-
331 called huddle-test and were used to accurately reconstitute the instrument responses. Their
332 overall self-noise resides around the global minimum noise level (Peterson, 1993) over a
333 wide frequency range, through which they become versatile and useful for a wide range
334 of seismological applications, such as seismotectonics in local and regional distances, noise
335 tomography, ambient noise studies and applied geophysics. In direct comparison to stan-
336 dard instruments in use for decades for seismological surveys, the nodes show at least
337 the same performance levels, even beyond their natural frequency, while having the ad-
338 vantage of highly reduced purchasing costs, weight, and installation and dismantling time.
339 This study endorses the use of SmartSolo nodes as low-budget alternatives, either for
340 Large N installations or for research groups that have limited financial resources to per-
341 form seismotectonic or ambient noise studies using more expensive but higher-quality
342 seismic sensors.

343 **Data and Resources**

344 All seismic waveforms processed for this study have been obtained at the Royal Obser-
 345 vatory of Belgium and are available alongside with the publicly available python codes
 346 at <https://gitlab-as.oma.be/martinz/smartsolo-nodes-paper>.

347 **Declaration of Competing Interests**

348 The authors declare no competing interests.

349 **Acknowledgments**

350 The authors want to thank the staff of the Seismology-Gravimetry section at the
 351 Royal Observatory of Belgium for constructive discussions during various steps of the
 352 study. A special thanks goes to Giovanni Rapagnani for his help in data analysis and
 353 reviewing the manuscript. MZ has been funded by two projects of the Belgian Science
 354 Policy Office (BELSPO) including (1) the Belgian contribution to EPOS (FSIRI/33/EP1)
 355 and (2) the BRAIN-be 2.0 GeoCamb project (B2/191/P1/GEOCAMB).

356 **References**

- 357 Ahrens, J., Hendrickson, B., Long, G., Miller, S., Ross, R., & Williams, D. (2011).
 358 Data-intensive science in the us doe: case studies and future challenges. *Comput-*
 359 *ing in Science & Engineering*, 13(6), 14–24.
- 360 Anthony, R. E., Ringler, A. T., Wilson, D. C., & Wolin, E. (2019). Do low-cost
 361 seismographs perform well enough for your network? an overview of laboratory
 362 tests and field observations of the osop raspberry shake 4d. *Seismological Research*
 363 *Letters*, 90(1), 219–228.
- 364 Arrowsmith, S., Trugman, D., MacCarthy, J., Bergen, K., Lumley, D., & Magnani,
 365 M. (2022). Big data seismology. *Reviews of Geophysics*, 60(2), e2021RG000769.
- 366 Bergen, K. J., Chen, T., & Li, Z. (2019). Preface to the focus section on machine
 367 learning in seismology. *Seismological Research Letters*, 90(2A), 477–480.
- 368 Bozdag, E., Lefebvre, M., Lei, W., Peter, D., Smith, J., Komatitsch, D., & Tromp,
 369 J. (2014). Big data and high-performance computing in global seismology. In *Egu*
 370 *general assembly conference abstracts* (p. 16606).
- 371 Brenguier, F., Kowalski, P., Ackerley, N., Nakata, N., Boué, P., Campillo, M., . . .

- 372 Chaput, J. (2015, 11). Toward 4D Noise-Based Seismic Probing of Volcanoes:
 373 Perspectives from a Large-N Experiment on Piton de la Fournaise Volcano. *Seis-*
 374 *mological Research Letters*, 87(1), 15-25. doi: 10.1785/0220150173
- 375 Calais, E., Symithe, S., Monfret, T., Delouis, B., Lomax, A., Courboux, F., ...
 376 others (2022). Citizen seismology helps decipher the 2021 haiti earthquake.
 377 *Science*, 376(6590), 283-287.
- 378 Castellanos, J. C., & Clayton, R. W. (2021). The fine-scale structure of long beach,
 379 california, and its impact on ground motion acceleration. *Journal of Geophysical*
 380 *Research: Solid Earth*, 126(12), e2021JB022462.
- 381 Chatelain, J.-L., Gueguen, P., Guillier, B., Frechet, J., Bondoux, F., Sarrault, J.,
 382 ... Neuville, J.-M. (2000). Cityshark: A user-friendly instrument dedicated
 383 to ambient noise (microtremor) recording for site and building response studies.
 384 *Seismological Research Letters*, 71(6), 698-703.
- 385 Chen, K. H., Bossu, R., & Liang, W.-T. (2020). *The power of citizen seismology:*
 386 *Science and social impacts* (Vol. 8). Frontiers Media SA.
- 387 Chmiel, M., Mordret, A., Boué, P., Brenguier, F., Lecocq, T., Courbis, R., ...
 388 Van der Veen, W. (2019, 05). Ambient noise multimode Rayleigh and Love
 389 wave tomography to determine the shear velocity structure above the Groningen
 390 gas field. *Geophysical Journal International*, 218(3), 1781-1795. Retrieved from
 391 <https://doi.org/10.1093/gji/ggz237> doi: 10.1093/gji/ggz237
- 392 Dean, T., & Sweeney, D. (2019). Recent advances in nodal land seismic acquisition
 393 systems. *ASEG Extended Abstracts*, 2019(1), 1-4.
- 394 Dean, T., Tulett, J., & Barnwell, R. (2018). Nodal land seismic acquisition: The
 395 next generation [Journal Article]. *First Break*, 36(1), 47-52. doi: [https://doi.org/](https://doi.org/10.3997/1365-2397.n0061)
 396 [10.3997/1365-2397.n0061](https://doi.org/10.3997/1365-2397.n0061)
- 397 De Plaen, R. S., Márquez-Ramírez, V. H., Pérez-Campos, X., Zuñiga, F. R.,
 398 Rodríguez-Pérez, Q., Gómez González, J. M., & Capra, L. (2021). Seismic
 399 signature of the covid-19 lockdown at the city scale: a case study with low-cost
 400 seismometers in the city of querétaro, mexico. *Solid Earth*, 12(3), 713-724.
- 401 GEOFON Data Centre. (1993). *Geofon seismic network*. Deutsches Geo-
 402 Forschungszentrum GFZ. Retrieved from [http://geofon.gfz-potsdam.de/](http://geofon.gfz-potsdam.de/doi/network/GE)
 403 [doi/network/GE](http://geofon.gfz-potsdam.de/doi/network/GE) doi: 10.14470/TR560404
- 404 Hand, E. (2014). *A boom in boomless seismology*. American Association for the Ad-

- 405 vancement of Science.
- 406 Havskov, J., & Alguacil, G. (2015). *Instrumentation in earthquake seismology*.
 407 Springer. (Publication Title: Instrumentation in Earthquake Seismology) doi:
 408 10.1007/978-3-319-21314-9
- 409 Karplus, M., & Schmandt, B. (2018). Preface to the focus section on geophone array
 410 seismology. *Seismological Research Letters*, *89*(5), 1597–1600.
- 411 Kong, Q., Trugman, D. T., Ross, Z. E., Bianco, M. J., Meade, B. J., & Gerstoft, P.
 412 (2019). Machine learning in seismology: Turning data into insights. *Seismological*
 413 *Research Letters*, *90*(1), 3–14.
- 414 Lecocq, T., Hicks, S. P., Van Noten, K., Van Wijk, K., Koelemeijer, P., De Plaen,
 415 R. S., ... others (2020). Global quieting of high-frequency seismic noise due to
 416 covid-19 pandemic lockdown measures. *Science*, *369*(6509), 1338–1343.
- 417 Lunedei, E., & Malischewsky, P. (2015). A review and some new issues on the the-
 418 ory of the h/v technique for ambient vibrations. *Perspectives on European earth-*
 419 *quake engineering and seismology*, 371–394.
- 420 MacCarthy, J., Marciullo, O., & Trabant, C. (2020). Seismology in the cloud: A new
 421 streaming workflow. *Seismological Research Letters*, *91*(3), 1804–1812.
- 422 Molnar, S., Sirohey, A., Assaf, J., Bard, P.-Y., Castellaro, S., Cornou, C., ... others
 423 (2022). A review of the microtremor horizontal-to-vertical spectral ratio (mhvsr)
 424 method. *Journal of Seismology*, 1–33.
- 425 Nakamura, Y. (1989). A method for dynamic characteristics estimation of subsur-
 426 face using microtremor on the ground surface. *Railway Technical Research Insti-*
 427 *tute, Quarterly Reports*, *30*(1).
- 428 Obermann, A., Sánchez-Pastor, P., Wu, S., Wollin, C., Baird, A. F., Isken, M. P.,
 429 ... Wiemer, S. (2022, July). Combined Large-N Seismic Arrays and DAS Fiber
 430 Optic Cables across the Hengill Geothermal Field, Iceland. *Seismological Research*
 431 *Letters*. Retrieved 2022-08-17, from <https://doi.org/10.1785/0220220073> doi:
 432 10.1785/0220220073
- 433 Peterson, J. R. (1993). *Observations and modeling of seismic background noise*
 434 (Tech. Rep.). US Geological Survey. doi: 10.3133/ofr93322
- 435 Quinteros, J., Carter, J. A., Schaeffer, J., Trabant, C., & Pedersen, H. A. (2021).
 436 Exploring approaches for large data in seismology: User and data repository per-
 437 spectives. *Seismological Research Letters*, *92*(3), 1531–1540.

- 438 Ringler, A., Hutt, C., Evans, J., & Sandoval, L. (2011). A comparison of seismic in-
 439 strument noise coherence analysis techniques. *Bulletin of the Seismological society*
 440 *of America*, 101(2), 558–567.
- 441 Ringler, A. T., Anthony, R. E., Karplus, M., Holland, A., & Wilson, D. C. (2018).
 442 Laboratory tests of three z-land fairfield nodal 5-hz, three-component sensors.
 443 *Seismological Research Letters*, 89(5), 1601–1608.
- 444 Ringler, A. T., Sleeman, R., Hutt, C. R., & Gee, L. S. (2014). Seismometer self-
 445 noise and measuring methods. In *Encyclopedia of earthquake engineering* (pp. 1–
 446 13). Springer Berlin Heidelberg. doi: 10.1007/978-3-642-36197-5_175-1
- 447 Roux, P., Bindi, D., Boxberger, T., Colombi, A., Cotton, F., Douste-Bacque, I., ...
 448 Pondaven, I. (2018, 01). Toward Seismic Metamaterials: The METAFORÉT
 449 Project. *Seismological Research Letters*, 89(2A), 582-593. doi: 10.1785/
 450 0220170196
- 451 Royal Observatory of Belgium. (1985). *Belgian seismic network*. International Fed-
 452 eration of Digital Seismograph Networks. Retrieved from [https://www.fdsn.org/
 453 networks/detail/BE/](https://www.fdsn.org/networks/detail/BE/) doi: 10.7914/SN/BE
- 454 Scherbaum, F. (2006). *Of poles and zeros: Fundamentals of digital seismology*
 455 (Vol. 15). Springer Science & Business Media.
- 456 Sleeman, R., Van Wetteum, A., & Trampert, J. (2006). Three-channel correlation
 457 analysis: A new technique to measure instrumental noise of digitizers and seismic
 458 sensors. *Bulletin of the Seismological Society of America*, 96(1), 258–271.
- 459 Subedi, S., Hetényi, G., Denton, P., & Sauron, A. (2020). Seismology at school
 460 in nepal: a program for educational and citizen seismology through a low-cost
 461 seismic network. *Frontiers in Earth Science*, 73.
- 462 Van Noten, K., Lecocq, T., Goffin, C., Meyvis, B., Molron, J., Debacker, T. N., &
 463 Devleeschouwer, X. (2022). Brussels’ bedrock paleorelief from borehole-controlled
 464 power laws linking polarised h/v resonance frequencies and sediment thickness.
 465 *Journal of Seismology*, 26(1), 35–55.
- 466 Wathelet, M., Chatelain, J.-L., Cornou, C., Giulio, G. D., Guillier, B., Ohrnberger,
 467 M., & Savvaidis, A. (2020). Geopsy: A user-friendly open-source tool set for
 468 ambient vibration processing. *Seismological Research Letters*, 91(3), 1878–1889.

469 **Full mailing address for each author**

470 Martin Zeckra - martin.zeckra@seismology.be

471 Koen Van Noten - koen.vannoten@seismology.be

472 Thomas Lecocq - thomas.lecocq@seismology.be